PAPER

Check for updates

Degradation of ciprofloxacin by TiO$_2$/Fe$_2$O$_3$/zeolite catalyst-activated persulfate under visible LED light irradiation

Minmin Liu,[a] Lin Zhang,[b] Bei-dou Xi,[d] Shuili Yu,[c] Xiaojun Hu ◍ *[a] and Li-an Hou*[b]

The activation of persulfate (PS) by metal catalysts under visible light is expected to offer a promising oxidation reaction for the removal of contaminants from water. Herein, we investigated activated PS systems under visible light irradiation for the generation of reductive species to decompose ciprofloxacin (CIP). Improved PS activation using TiO$_2$/Fe$_2$O$_3$/zeolite ((n)TiFeZ) under visible light irradiation favorably leads the reaction to generate reductive radicals. The enhanced degradation efficiencies of the (n)TiFeZ–PS system for CIP removal was due to the extended absorbance in the visible-light region and improved space separation of photo-induced charge carriers. The (4)TiFeZ catalyst exhibited better performance for CIP removal as compared to the other samples. The CIP was completely degraded in 120 min using 1 g L^{-1} (4)TiFeZ and 5.0 mM PS at pH 7.0. The characterization and electron paramagnetic resonance (EPR) of (n)TiFeZ suggested that CIP was mainly degraded by surface-adsorbed radicals generated from the reaction between PS and Fe(II) on the samples under visible light. The reductive systems coupled with (n)TiFeZ exhibited high CIP degradation efficiency and high potential for the decomposition of other antibiotic compounds.

1. Introduction

Ciprofloxacin (CIP; C$_{17}$H$_{18}$O$_3$N$_3$F) is one of the most frequently prescribed human-use fluoroquinolone all over the world.[1] It was often detected in the effluent of wastewater treatment plants due to its high aqueous solubility under various pH conditions and high stability in wastewater. Various treatment processes have been applied to remove CIP from water. Especially, advanced oxidation processes (AOPs) contain promising, efficient, and environmentally friendly methods involving the generation of highly reactive radicals to decompose organic pollutants. Thus, AOPs are attractive treatment methods for CIP removal. Among AOPs, activated persulfate (PS, S$_2$O$_8^{2-}$) oxidation is gaining importance in water treatment because PS is stable at ambient temperatures, highly soluble in water, and much cheaper than peroxymonosulfate (PMS) and H$_2$O$_2$.[1–4]

Various iron-bearing catalysts through the incorporation of iron into various supports, such as mesoporous silica, clay, and carbon, have been explored to activate PS to generate sulfate radicals.[5–7] The application of supports is beneficial for high mineralization of organic contaminants and easy separation from treated wastewater without causing secondary metal ion pollution. CIP has multiple ionisable functional groups. At neutral pH, the largely dominant species is zwitterionic, whereas the cationic form and the anionic form predominately in acidic and in basic solutions, respectively. Thus, it can exist as a cation, zwitterion, and anion under aqueous pH conditions. Previous studies show that CIP molecules react with supports by cation exchange rather than cation bridging or surface complexation.[8] Depending on the regularly arranged cavities and crystal structure of zeolites, zeolites can be used as hosts to accommodate nano-sized iron materials and support to remove CIP.[9] Various physical and chemical methods have been explored to activate PS to generate sulfate radicals.[10] Especially, activation under light irradiation is more attractive than thermal or chemical activation for producing SO$_4^{-\bullet}$ with high efficiency.

Semiconductor materials have played an important role in activation under light irradiation. TiO$_2$ has been applied to photocatalytic processes due to its non-toxicity, low cost, and high stability.[11–13] The major limitations of TiO$_2$ are its difficult separation from water and large E_g value (E_g = 3.2 eV), which inhibits the absorption of the visible light. Therefore, to increase the visible light absorption of TiO$_2$, its coupling with lower band gap semiconductors, such as Fe$_2$O$_3$, Cu$_2$O, CuO, CdSe, and CdTe, can spatially separate electron–hole pairs and thereby decrease the recombination rates. The TiO$_2$–Fe$_2$O$_3$

^{a}School of Chemical and Environmental Engineering, Shanghai Institute of Technology, 100 Haiquan Road, Shanghai, P. R. China. E-mail: hxjsit@126.com; Fax: +86 13045681913; Tel: +86 13045681913

^{b}Key Laboratory of Biomass Chemical Engineering of MOE, College of Chemical and Biological Engineering, Zhejiang University, Hangzhou 310027, P. R. China

^{c}State Key Laboratory of Pollution Control and Resource Reuse, School of Environmental Science and Engineering, Tongji University, 1239 Siping Road, Shanghai 200092, P. R. China

^{d}State Key Laboratory of Environmental Criteria and Risk Assessment, China Research Academy of Environmental Science, Beijing 200012, P. R. China

composite can be more efficient photocatalysts than pure TiO_2 towards organic compound degradation in the UV-vis region of the spectrum due to the narrow band gap ($E_g = 2.2$ eV), low cost, and high stability of Fe_2O_3.[14] To date, various TiO_2-supported catalysts have been developed to activate PS under UV light for the degradation of organics. However, to the best of our knowledge, very limited information on TiO_2/Fe_2O_3-supported zeolite/PS oxidation of CIP in water under visible light is available although it is a likely option for the treatment of CIP-induced water pollution. It is interesting to explore the activation of persulfate with TiO_2/iron-modified zeolite under visible light irradiation for CIP removal.

In addition, the visible light-emitting diodes (LEDs) extensively used in interior and exterior lighting offers a new alternative to conventional light sources due to their narrow spectrum of light, long life span, high spectral purity, small size, and lack of requirement for cooling. Thus, they appear ideal candidates for environmental remediation procedures with reduced power consumption and greater potential for flexible configuration.

To date, many studies have been reported on the UV/PS, UV-vis/catalyst/PS, UV or vis/catalyst/H_2O_2 processes; however, studies on the vis/catalyst/PS system have not been reported. It is the first time that TiO_2/Fe_2O_3/zeolite catalysts have been combined with PS and vis light for the removal of non-biodegradable organics. In this study, we fabricated TiO_2/Fe_2O_3-supported zeolites ((n) TiFe-Z) as catalysts to activate persulfate under visible LED light irradiation. The mechanisms of PS activation and radical revolution were investigated, and the possible degradation pathway was revealed by identification of the reaction intermediates. Moreover, the effects of pH, catalyst loading, PS dosage, and radical scavengers on the oxidation efficiencies were systematically investigated. This study was aimed at providing a green, novel, and highly-efficient PS activation technology for sulfate radical-based oxidation.

2. Experimental

2.1 Materials and chemicals

CIP hydrochloride was purchased from the Sigma-Aldrich Corporation. Commercial P25 TiO_2 (80% anatase and 20% rutile, BET = *ca.* 270 m^2 g^{-1}) was purchased from Degussa. Nanoscale zero valent iron particles Fe^0 (NZVI) were purchased from Fisher Scientific. The size of NZVI was 50 nm. Sodium silicate solution, sodium aluminate, sodium hydroxide, hydrochloric acid, and ferric nitrate were purchased from Fisher Scientific. Sodium oxalate ($Na_2C_2O_4$), benzoquinone (BQ), ascorbic acid (AsA), dimethyl sulfoxide (DMSO), methanol, and 5,5-dimethyl-1-pyrroline-*N*-oxide (DMPO) were purchased from Aladdin, China. All the chemicals were of analytical grade and used without further purification. Milli-Q ultrapure water (18.2 MU cm) was used for all the experiments.

2.2 Synthesis of (n)TiFe-Z

Sodium silicate, sodium aluminate, and sodium hydroxide were mixed in water, and a white gel was formed. The molar ratio of

$Na_2O : Al_2O_3 : SiO_2 : H_2O$ was $7.15 : 1 : 2.2 : 122$. The gel was heated to boiling for 1 h to produce the precursors of zeolite X. Then, 4 wt% of TiO_2 and various weight percentages of NZVI (4, 8, 16, and 24 wt%) were added to the precursors of zeolite X and then stirred to be homogenized. The gel was crystallized by the Teflon-lined stainless autoclave at 343 K for 3 h and then at 368 K for 2 h. The autoclave was naturally cooled down to room temperature. Finally, the product was washed with deionized water and calcined at 673 K for 3 h to obtain the TiO_2/Fe_2O_3-supported zeolites ((n) TiFeZ). The value of n, which was 1, 2, 4, and 6, presented the ratio of the weight percentage of NZVI to that of the TiO_2. The zeolite X was prepared by the same method without adding TiO_2.

2.3 Characterization and analysis

A D/MAX-2500 diffractometer (Rigaku, Japan) was applied to characterize the crystalline phases of the final products using Ni-filtered CuK radiation and a scan range of 10–80° at a scanning rate of 0.02° s^{-1}. The Brunauer–Emmett–Teller (BET) surface areas were characterized using a N_2 adsorption–desorption isotherm (ASAP-2020 Micromeritics Co., USA) and calculated from the linear part of the BET plot. The sample structure was observed using a JEOL H-8100 field emission scanning electron microscope (FESEM). Photoluminescence (PL) spectra of the sample was obtained using a Perkin Elmer LS55 fluorescence spectrometer with the excitation wavelength of 320 nm at room temperature. The sample was pressed into a thin disk and fixed on a quartz cell. The infrared absorption spectra were obtained by a Nicolet 6700 Fourier transform infrared (FT-IR) spectrophotometer and after the spectrum scan of the blank pure KBr pellet. The UV-vis diffuse reflectance spectroscopy (UV-vis DRS) measurements were conducted using a Hitachi UV-3600 UV-vis spectrophotometer in the range of 200–800 nm, and $BaSO_4$ was used as a reflectance standard. X-ray photoelectron spectroscopy (XPS) was performed using an ESCA 3000 spectrometer to characterize the chemical state of the elements in the samples. The CIP concentration was determined by ultra-performance liquid chromatography (UPLC) (Waters, USA). The flow rate was 0.8 mL min L^{-1} and the wavelength of the ultraviolet (UV) detector was set at 355 nm. The mobile phase was 1% ethylic acid solution (80%) and methanol (20%). The correlation coefficient of the standard curve ($n = 10$) was more than 0.999. All the TC concentrations were measured in triplicate and mean values were used. The iron concentration in the solution was measured by inductively coupled plasma mass spectrometry (ICP-MS) using Agilent HP 4500.

2.4 The batch experiments

The CIP degradation performance of samples was evaluated under 50 W 455 nm LED light irradiation. The experiments were carried out in a reactor containing 0.1 g sample, 100 mL 500 mg L^{-1} aqueous solution of CIP, and 5 mM $Na_2S_2O_8$ solution. The pH of the TC solution was adjusted by adding one or two drops of 0.1 mol L^{-1} HCl or NaOH solution. The distance between the LED light source and the reactor was 5 cm. Then,

the reactor was exposed to the LED light irradiation. The reactor was continuously agitated by a magnetic stir bar. All the experiments were conducted in duplicates, and the results showed that the experimental errors were less than 5%.

3. Results and discussion

3.1 Physicochemical characterization

3.1.1 XRD.
The XRD profiles of (1)TiFeZ, (2)TiFeZ, (4)TiFeZ, (6)TiFeZ, and zeolite X are shown in Fig. 1. The signal peak at 25.4° indicated the planes of anatase.[15] The most intense peaks of the anatase phase (48.0° and 54.5°) can also be identified in the pattern of the sample (n)TiFeZ, overlapping with the zeolite reflections. The structures of zeolite X were not altered by TiO$_2$ and NZVI loading because no significant shift in the zeolite X peaks of (n)TiFeZ was observed as compared to that of pure zeolite X.

The characteristic peak of NZVI was observed at 45°.[16] The intensity of the reflection at 45° was increased with the

increasing weight percentage of NZVI. This indicated that some NZVI were coated on the surface of the zeolite X. As TiO$_2$ and NZVI loading was increased, the diffraction peaks of TiO$_2$ and NZVI became wider and sharper.

3.1.2 FESEM.
The FESEM images of zeolite X and (4)TiFeZ are shown in Fig. 2. The particle size was uniform and about 4 mm. The morphology of (4)TiFeZ was different from that of zeolite X. In addition, the surface of (4)TiFeZ was rough, and the small particles were coated on the surface of (4)TiFeZ; this indicated that some of TiO$_2$ and NZVI particles were immobilized on the surface of (4)TiFeZ.

3.1.3 Specific surface area and pore diameter.
As shown in Table 1, the specific surface area of (n)TiFeZ increased from 0.0844 to 0.1837 m^2 g^{-1} as the weight percentage of TiO$_2$ increased. The average pore diameters of the samples were between 0.743 and 0.969 nm, and the average pore diameter of zeolite X was 0.743 nm. The impregnation of NZVI and TiO$_2$ had an influence on the specific surface areas and pore diameters and volumes of the samples.

3.1.4 UV-vis DRS spectra.
As shown in Fig. 3, the absorbance of Ag/AgCl/(x)Fe-ZX in the visible light region was enhanced as the weight percentage of NZVI increased.

3.1.5 Photoluminescence (PL).
As shown in Fig. 4, the PL spectrum intensity of the (n)TiFeZ samples decreased when the weight percentage of NZVI increased. There was a large decrease in the PL intensity of (n)TiFeZ. This suggested that as the weight percentage of NZVI increased, the recombination of the photoelectron and hole pairs of (n)TiFeZ was more inhibited. (6)TiFeZ possesses much better optical and photoluminescence behaviors than the other samples.

3.2 Evaluation of CIP degradation

3.2.1 The effect of NZVI on CIP adsorption.
Table 2 shows the maximum adsorption capacities Q_{max} of (n)TiFeZ and the Langmuir adsorption constants (K_{ads}). The correlation coefficients R^2 of the linear form of the Langmuir model were close to 1. This suggested that the Langmuir model could describe CIP adsorption. It also showed that the CIP adsorption process occurred on the homogeneous surface by monolayer adsorption.[17] The Q_{max} of (n)TiFeZ increased from 354.6 mg g^{-1} to 435.2 mg g^{-1} when the weight percentage of NZVI was increased from 1% to 4%. However, the Q_{max} of (n)TiFeZ decreased as the weight percentage of NZVI was increased from 4% to 6%.

3.2.2 Comparison of CIP removal efficiency by (n)TiFeZ.
As shown in Fig. 5A and B, the photocatalytic performances of the prepared samples were studied by the removal of CIP under visible light illumination with and without PS. Without any catalyst and PS, CIP was fairly stable, and the self-degradation of CIP through photolysis was negligible (<0.1% over 4 h).

The pseudo-first order equation could be applied to describe the CIP photocatalytic kinetics by the catalysts. The equation is as follows:

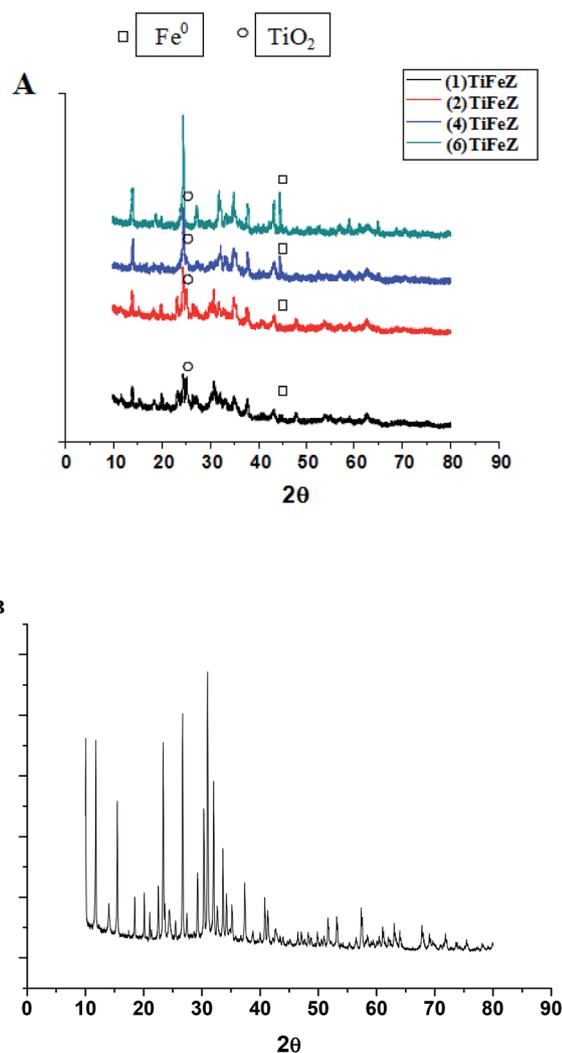$$\ln\left(\frac{C_0}{C}\right) = k_3 t \qquad (1)$$

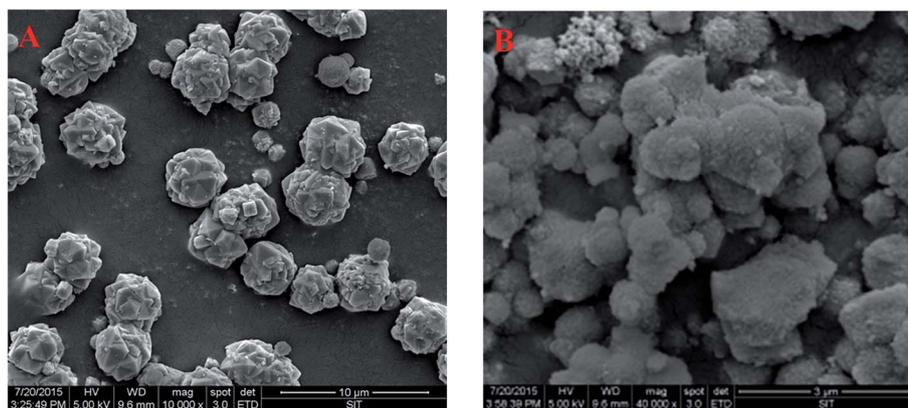Fig. 1 (A) XRD patterns of (1)TiFeZ, (2)TiFeZ, (4)TiFeZ and (6)TiFeZ; (B) XRD pattern of zeolite X.

Fig. 2 FESEM images of (A) zeolite X and (B) (4)TiFeZ.

Table 1 Specific surface area, pore diameters, and pore volumes of the samples

Samples	S_{BET} (m^2 g^{-1})	Pore diameter (nm)	Pore volume (cm^3 g^{-1})
Zeolite X	0.0844	0.743	0.288
(1)TiFeZ	0.0932	0.789	0.315
(2)TiFeZ	0.1168	0.818	0.346
(4)TiFeZ	0.1445	0.885	0.375
(6)TiFeZ	0.1837	0.969	0.411
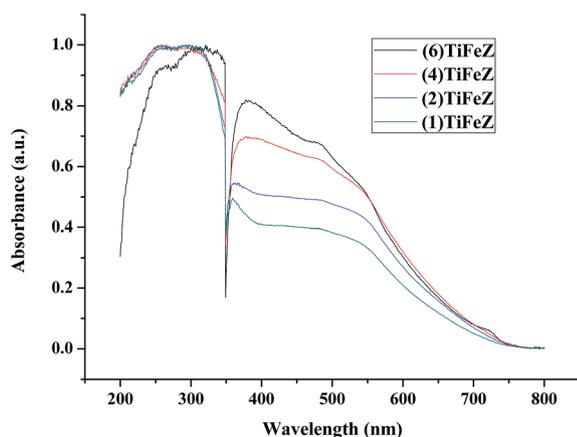
Fig. 3 UV–vis diffuse reflectance spectra of (n)TiFeZ.

where C_0 is the initial concentration of CIP (mg L^{-1}), C stands for the CIP concentration (mg L^{-1}) at reaction time t, and k_3 represents the pseudo-first order rate constant (min^{-1}).

In the present study, the pseudo-first-order kinetics model, as shown in eqn (1), was used to study the degradation of CIP by the photocatalyst under visible light illumination without PS (Fig. 5C) and with PS (Fig. 5D). The values of correlation coefficient R^2 were above 0.9, confirming that the removal profiles in all the cases could be well expressed with the pseudo-first-order kinetics. From Fig. 5C, based on the equation, the slopes of the fitted lines were the k_3 values. The k_3 values were calculated to be 0.356, 0.405, 0.509, and 0.474 for (1)TiFeZ, (2)TiFeZ, (4)TiFeZ,

and (6)TiFeZ, respectively. Compared with those obtained using other samples, the rate constant of CIP degradation obtained using (4)TiFeZ was higher.

From Fig. 5D, the k_3 values were calculated to be 0.3966, 0.4816, 0.7134, and 0.6013 for (1)TiFeZ, (2)TiFeZ, (4)TiFeZ, and (6)TiFeZ, respectively. The order of the CIP removal efficiencies by (n)TiFeZ under visible light was (4)TiFeZ > (6)TiFeZ > (2)TiFeZ > (1)TiFeZ. The k_3 value of (n)TiFeZ-PS under visible light was more than that of (n)TiFeZ-PS in the dark. This indicated that the PS activation was promoted under visible light.

3.2.3 The effect of pH. The (n)TiFeZ sample was applied for the pH studies because its CIP degradation efficiency was more
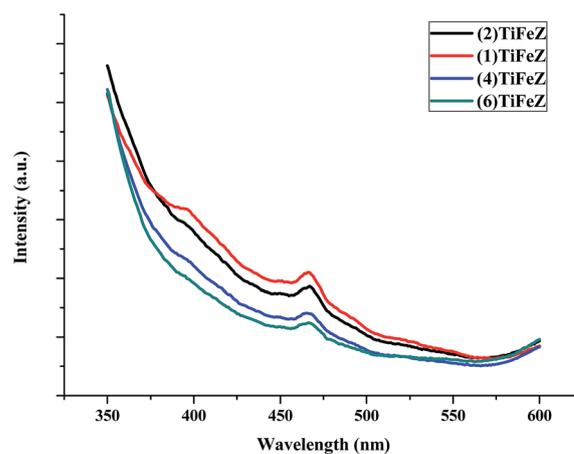

Fig. 4 PL spectra of (n)TiFeZ.

Table 2 The Langmuir isotherm model parameters of CIP adsorption on (n)TiFeZ (dosage of catalysts, 1 g L^{-1}; pH, 7.0)

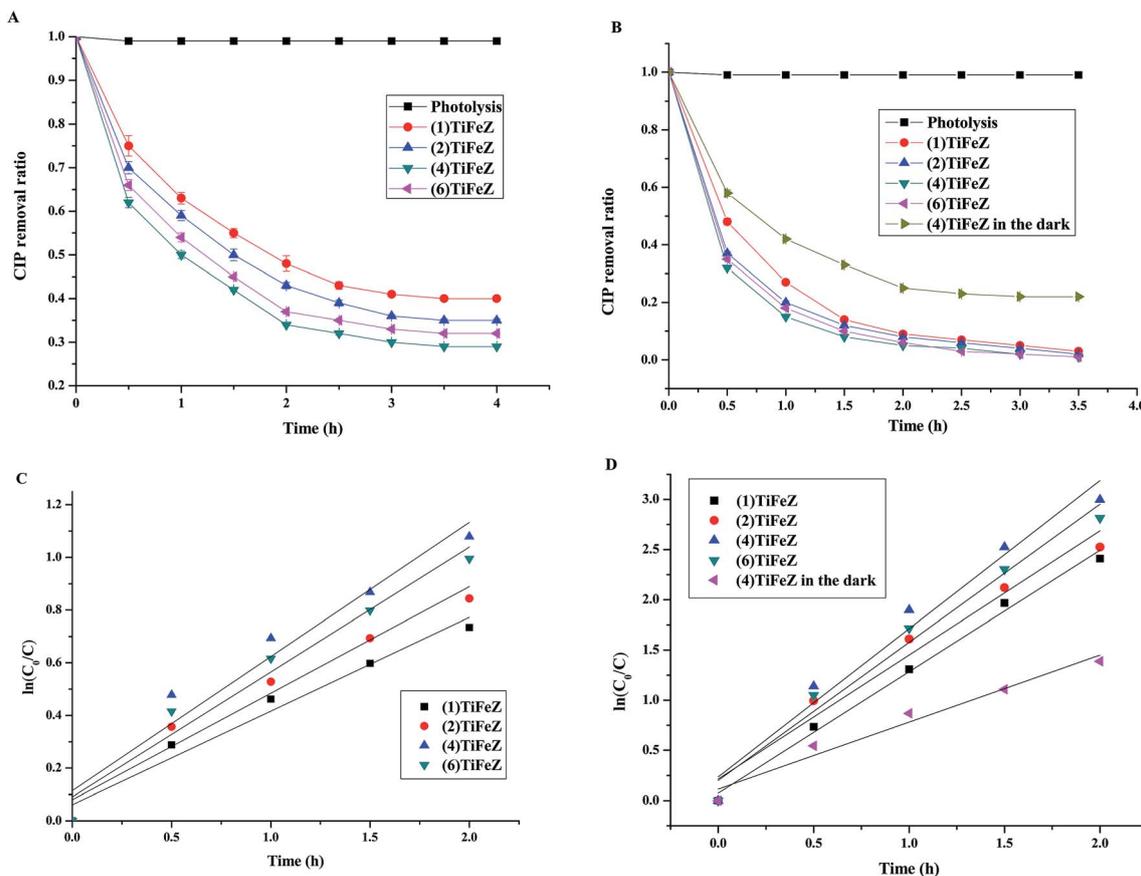| Samples	Q_{max} (mg g^{-1})	K_{ads} (L mg^{-1})	R^2
Zeolite X	354.6	1.21	0.945
(1)TiFeZ	382.5	3.23	0.953
(2)TiFeZ	401.3	4.31	0.965
(4)TiFeZ	435.2	5.12	0.971
(6)TiFeZ	408.6	4.37	0.982

Fig. 5 The efficiencies of CIP removal by the catalysts under visible-light irradiation without PS (A) and with PS (B); photocatalytic degradation reaction kinetics for catalysts without PS (C) and with PS (D) (initial CIP concentration, 500 mg L^{-1}; dosage of catalysts, 1 g L^{-1}; and pH, 7).
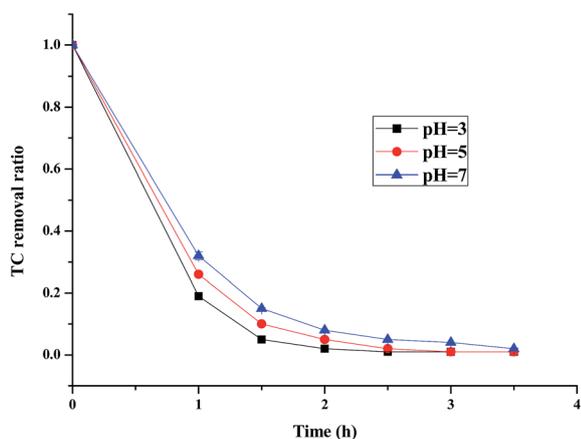

Fig. 6 Effects of pH on the degradation of CIP (CIP concentration, 500 mg L^{-1}; dosage of catalyst, 1 g L^{-1}).

than that of the other samples. Fig. 6 presents the effect of pH on the CIP degradation efficiency of (*n*)TiFeZ. As the pH increased from 3 to 7, the CIP degradation efficiency decreased. It showed that as the pH was decreased, the breakdown of persulfate into sulfate free radicals could be further promoted. More SO$_4^{-\bullet}$ radicals were produced to enhance the TC degradation efficiency. The reaction equations are shown below:

$$S_2O_8^{2-} + H^+ \rightarrow HS_2O_8^-$$

$$HS_2O_8^- \rightarrow SO_4^{2-} + H^+ + SO_4^{-\bullet}$$
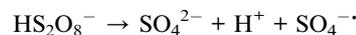
Fe^{2+} ions were more easily produced from NZVI at lower pH. The homogeneous Fe^{2+} ions activated persulfate by the following reaction:

$$Fe^{2+} + S_2O_8^{2-} \rightarrow Fe^{3+} + SO_4^{-\bullet} + SO_4^{2-}$$

The precipitation of Fe^{2+} and Fe^{3+} ions might occur at pH 5.5–7.5.[14] When the pH increased, more sulfate radicals could be transformed to hydroxyl radicals through the following reaction:

$$SO_4^{-\bullet} + H_2O \rightarrow SO_4^{2-} + OH^\bullet + H^+$$

There were more sulfate radicals generated at lower pH and there were more hydroxyl radicals generated at higher pH. The reduction potential of the sulfate radicals was higher than that of the hydroxyl radicals at higher pH, and their reduction potentials were similar at lower pH. Thus, the CIP degradation efficiency decreased as the pH increased.
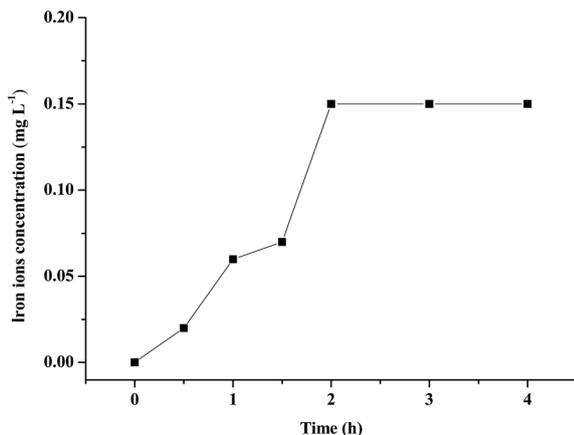
Fig. 7 Iron ion concentration in water during CIP degradation by (n) TiFeZ.

3.2.4 The stability of (n)TiFeZ. From Fig. 7, the iron ion concentration was measured during the process of CIP degradation. The maximum concentration of leached iron ion was only 0.15 mg L^{-1}, which was far below the European Union standard (2 mg L^{-1}); compared with the iron content of (n) TiFeZ, the content of leached iron ion was negligible. Thus, (n) TiFeZ is a sustainable and environmentally friendly catalyst.

3.3 Mechanism discussion

XPS could provide chemical state information of the surface components. According to the characterization results, there were NZVI particles coated on the surface of zeolite X. As shown in Fig. 8, the binding energies of 710.33 eV and 710.59 eV present the binding energies of Fe(II) and Fe(III) in the Fe 2p core level photoelectron spectra, respectively. It suggests that on the surface of (4)TiFeZ, the oxidation states of iron are +II and +III. The peak area ratios of Fe(III) to Fe(II) before and after CIP degradation were 9.12 and 7.22, respectively. This is because after the heterogeneous photocatalytic reaction, the proportion of Fe(III) was reduced as compared to that of Fe(II). Fe(III) could trap and transfer electrons and holes to inhibit the recombination of photo-excited holes and electrons. This suggested that at the interface between Fe(III) and TiO$_2$, there was effective heterojunction electric field produced to make the photo-generated electrons and holes significantly strengthened. It promoted the reaction between Fe(II) and S$_2$O$_8$$^{2-}$ ions. The separation of the photo-electrons and holes was significantly strengthened. The formation efficiency of SO$_4$$^{-\cdot}$ enhanced to make the photocatalytic efficiency increase.

The Na$_2$C$_2$O$_4$, BQ, AsA, and DMSO scavengers were applied to determine the type of reactive oxygen species (ROS) produced in the (n)TiFeZ-PS system. The various inhibitory effects of the different radical scavengers on CIP degradation are presented in Fig. 9. As BQ and Na$_2$C$_2$O$_4$ were added, there were remarkable inhibitory effects on CIP degradation. As AsA and DMSO were added, there were moderate effects. This indicated that $^\cdot$OH was one of the predominant oxidative species for oxidizing CIP, produced by the reaction between $^\cdot$O$_2$$^-$ and H$_2$O.[18] A moderate
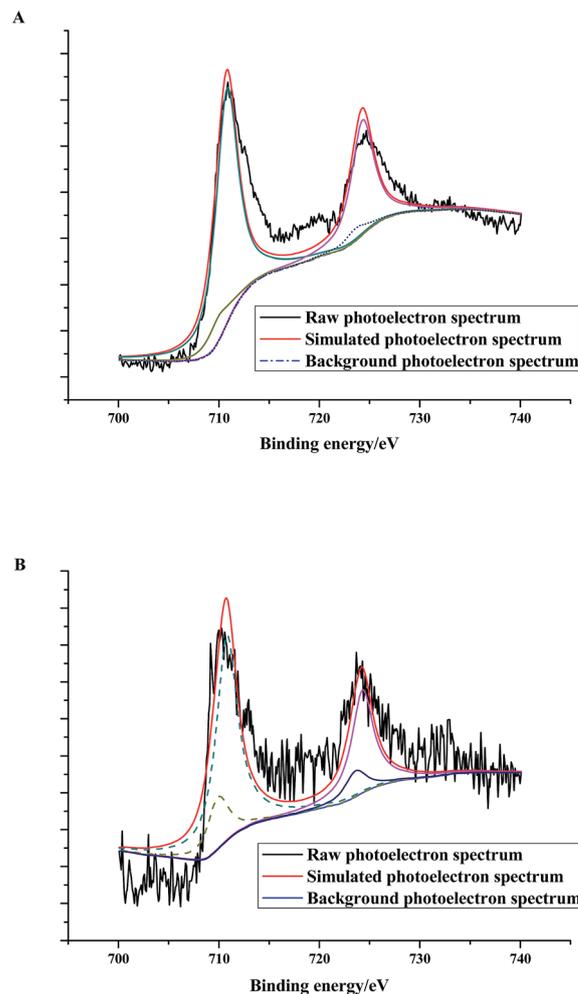

Fig. 8 Fe 2p core level photoelectron spectra of (n)TiFeZ before (A) and after (B) CIP degradation.

reduction in the CIP removal was observed as an h$^+$ scavenger (Na$_2$C$_2$O$_4$) was added that verified the contribution of h$^+$ in Cl^0 production for CIP oxidation.

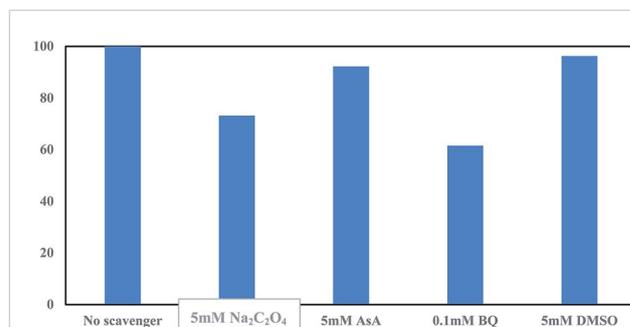The radical quenching experiments were first conducted to study whether the radicals were produced or not. As observed

Fig. 9 Effect of reactive radical scavengers on CIP degradation by (n) TiFeZ–PS after 3 h (CIP concentration, 500 mg L^{-1}; dosage of catalyst, 1 g L^{-1}; and pH, 7.0).
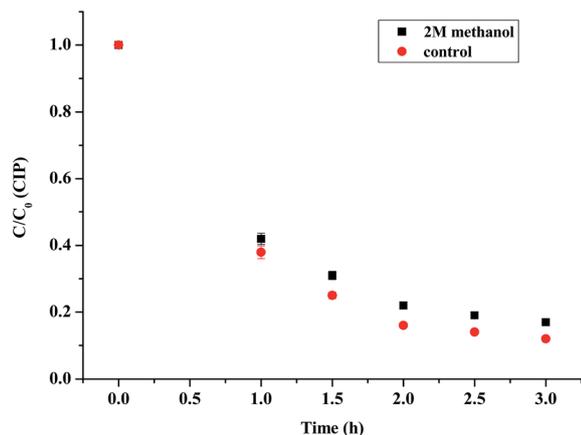
Fig. 10 Effects of methanol on CIP degradation by the (n)TiFeZ–PS system ([PS] = 5.0 mM, [(n)TiFeZ] = 1 g L^{-1}, and pH = 7.0).
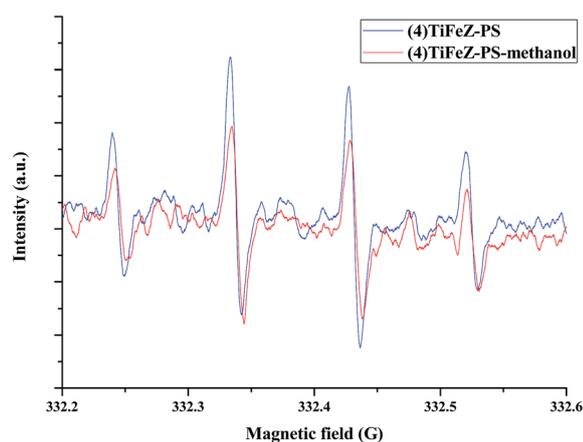

Fig. 11 EPR spectra *versus* time for supernatant of (4)TiFeZ–PS–CIP batch experiment ([PS] = 5.0 mM, [(n)TiFeZ] = 1 g L^{-1}, [DMPO] = 10 mM, and pH = 7.0).

from Fig. 10, when 2 M methanol was added to the reaction, the CIP removal was slightly decreased by 10%. The radicals produced were tested by EPR experiments. Furthermore, the free radicals such as superoxide radicals ($O_2^{\bullet-}$) and hydroxyl radicals ($OH^{\bullet}$) played a vital role in the photocatalytic process. The hydroxyl radicals generated in the photocatalytic process were measured by the EPR spectra. As shown in Fig. 11, more $OH^{\bullet}$ were generated by (4)TiFeZ–PS than by (4)TiFeZ–PS–methanol under visible light irradiation. This suggested that methanol did not capture the surface-adsorbed radicals completely[19] and 10% of CIP degradation was scavenged by the addition of 2 M methanol. This indicated that the CIP was degraded by the surface radicals.

In Fig. 12, a possible mechanism is proposed to explain the CIP degradation process by (n)TiFeZ. First, cationic CIP ions were adsorbed on the surface of (n)TiFeZ through an ion exchange reaction. Under visible light, TiO_2 and Fe_2O_3 nanoparticles on the surface of (n)TiFeZ could be excited to produce electron–hole (e^-/h^+) pairs (eqn (2)). During the process, the Fe(III)/Fe(II) cycle reaction enhances the space separation efficiency of the photo-induced charge carriers. This is because the impregnation with NZVI could cause a more efficient utilization of solar energy to accelerate this reaction. The conduction band (CB) electrons of TiO_2/Fe_2O_3 excited by visible light shifted to Fe(III) on the surface of (n)TiFeZ. Fe(III) could act as an electron trap to make the formation of Fe(II). Fe(II) was less stable than Fe(III) because of the half-filled stable d5 configuration. Therefore, the trapped charges could be released to generate stable Fe^{3+} ions (eqn (3)). During the process, it caused the formation of $^{\bullet}O_2^-$ and $SO_4^{-\bullet}$ superoxide radicals for the degradation of CIP (eqn (4) and (5)). The radicals $^{\bullet}O_2^-$ and $SO_4^{-\bullet}$ could react with H_2O to generate the $OH^{\bullet}$ radical (eqn (6) and (7)). The CIP molecule was oxidized by these superoxide species to intermediates and finally

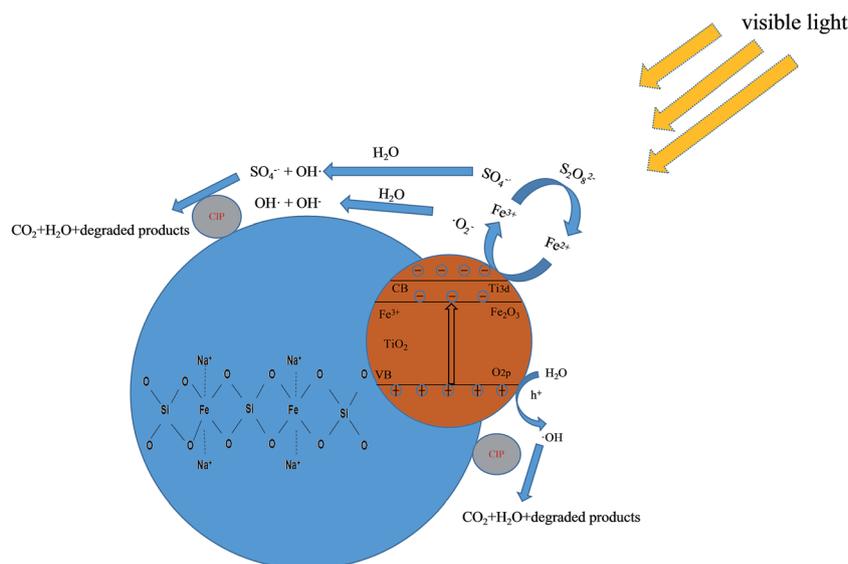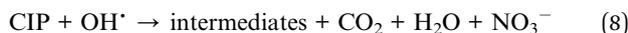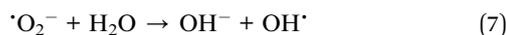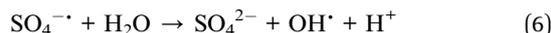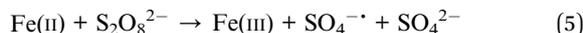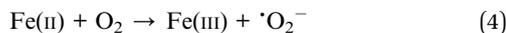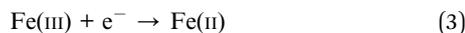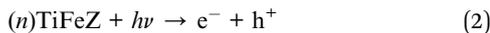**Fig. 12** Schematic of mechanisms of CIP degradation process by (n)TiFeZ–PS.

completely mineralized (eqn (8)). The reactions are presented by the following equations:

$$(n)TiFeZ + h\nu \rightarrow e^- + h^+ \tag{2}$$

$$Fe(III) + e^- \rightarrow Fe(II) \tag{3}$$

$$Fe(II) + O_2 \rightarrow Fe(III) + {}^\cdot O_2^- \tag{4}$$

$$Fe(II) + S_2O_8^{2-} \rightarrow Fe(III) + SO_4^{-\cdot} + SO_4^{2-} \tag{5}$$

$$SO_4^{-\cdot} + H_2O \rightarrow SO_4^{2-} + OH^\cdot + H^+ \tag{6}$$

$${}^\cdot O_2^- + H_2O \rightarrow OH^- + OH^\cdot \tag{7}$$

$$CIP + OH^\cdot \rightarrow intermediates + CO_2 + H_2O + NO_3^- \tag{8}$$

4. Conclusion

In conclusion, the catalysts ((n)TiFeZ) were synthesized by a facile hydrothermal method followed by the calcination method. The (4)TiFeZ catalyst showed better performance than other samples for CIP removal. The CIP degradation could be achieved in 2 h using 1 g L^{-1} (4)TiFeZ and 5.0 mM PS at pH 7.0. As the pH increased, the CIP degradation efficiency decreased. ${}^\cdot O_2^-$ and $SO_4^{-\cdot}$ were the predominant reactive oxygen species for CIP removal. After NZVI impregnation, the enhancement of the photocatalytic activity was mainly due to the extended absorption in the visible light region and the efficient space separation of photo-induced charge carriers. This study may expand the further development of zeolite-based heterogeneous catalysts for the degradation of organic pollutants through the activation of PS under visible light.

Conflicts of interest

There are no conflicts to declare.

Acknowledgements

References

1 M. M. Liu, B. D. Xi, L. A. Hou and S. L. Yu, Magnetic multi-functional nano-fly ash-derived zeolite composites for environmental applications, *J. Mater. Chem. A*, 2013, **1**, 12617–12626.

2 Y. X. Deng, M. Y. Xing and J. L. Zhang, An advanced TiO$_2$/Fe$_2$TiO$_5$/Fe$_2$O$_3$ triple-heterojunction with enhanced and stable visible-light-driven Fenton reaction for the removal of organic pollutants, *Appl. Catal., B*, 2017, **211**, 157–166.

3 M. M. Mokhtar, W. A. Bayoumy and M. E. Goher, Optimization of alpha - Fe$_2$O$_3$@Fe$_3$O$_4$ incorporated N-TiO$_2$ as super effective photocatalysts under visible light irradiation, *Appl. Surf. Sci.*, 2017, **412**, 668–682.

4 Y. Y. Liu, W. Jin, Y. P. Zhao, G. S. Zhang and W. Zhang, Enhanced catalytic degradation of methylene blue by α-Fe$_2$O$_3$/graphene oxide via heterogeneous photo-Fenton reactions, *Appl. Catal., B*, 2017, **206**, 642–652.

5 M. M. Liu, L. A. Hou, S. L. Yu and B. D. Xi, MCM-41 impregnated with A zeolite precursor: synthesis, characterization and tetracycline antibiotics removal from aqueous solution, *Chem. Eng. J.*, 2013, **223**, 678–687.

6 L. Cheng, S. F. Qiu, J. R. Chen, J. Shao and S. S. Cao, A practical pathway for the preparation of Fe$_2$O$_3$ decorated TiO$_2$ photocatalyst with enhanced visible-light photoactivity, *Mater. Chem. Phys.*, 2017, **190**, 53–61.

7 M. S. Rashid, G. M. Mehdipour and G. Mona, Photocatalytic degradation of diazinon under visible light using TiO$_2$/Fe$_2$O$_3$ nanocomposite synthesized by ultrasonic-assisted impregnation method, *Sep. Purif. Technol.*, 2017, **175**, 418–427.

8 X. M. Song, X. Zhou and C. X. Yuan, One-dimensionalFe$_2$O$_3$/TiO$_2$ photoelectrode and investigation of its photoelectric properties in photoelectrochemical cell, *Appl. Surf. Sci.*, 2017, **397**, 112–118.

9 M. M. Liu, B. D. Xi and L. A. Hou, Synthesis, characterization, and mercury adsorption properties of hybrid mesoporous aluminosilicate sieve prepared with flyash, *Appl. Surf. Sci.*, 2013, **273**, 706–716.

10 M. Ahmadi Golsefidi, F. Abbasi, M. Abrodi, Z. Abbasi and F. Yazarlou, Synthesis, characterization and photocatalytic activity of Fe$_2$O$_3$-TiO$_2$ nanoparticles and nanocomposites, *J. Nanostruct.*, 2016, **6**(1), 64–69.

11 M. M. Liu, L. A. Hou, Q. Li, X. J. Hu and B. D. Xi, Heterogeneous degradation of tetracycline by magnetic Ag/AgCl/modified zeolite X - persulfate system under visible light, *RSC Adv.*, 2016, **6**, 35216–35227.

12 W. Subramonian, T. Y. Wu and S. P. Chai, Photocatalytic degradation of industrial pulp and paper mill effluent using synthesized magnetic Fe$_2$O$_3$-TiO$_2$: treatment efficiency and characterizations of reused photocatalyst, *J. Environ. Manage.*, 2017, **187**, 298–310.

13 A. Banisharif, A. A. Khodadadi, Y. Mortazavi, A. Anaraki Firooz, J. Beheshtian, S. Agah and S. Menbari, Highly active Fe$_2$O$_3$-doped TiO$_2$ photocatalyst for degradation of trichloroethylene in air under UV and visible light irradiation: experimental and computational studies, *Appl. Catal., B*, 2015, **165**, 209–221.

14 M. M. Liu, L. A. Hou, B. D. Xi, Q. Li, X. J. Hu and S. L. Yu, Magnetically separable Ag/AgCl-zero valent iron particles modified zeolite X heterogeneous photocatalysts for tetracycline degradation under visible light, *Chem. Eng. J.*, 2016, **302**, 475–484.

15 Q. Y. Zhang, G. Y. Rao, J. Rogers and C. Y. Zhao, Novel anti-fouling Fe$_2$O$_3$/TiO$_2$ nanowire membranes for humic acid removal from water, *Chem. Eng. J.*, 2015, **271**, 180–187.

16 Y. B. Xia and L. W. Yin, Core-shell structured alpha-Fe_2O_3@TiO_2 nanocomposites with improved photocatalytic activity in the visible light region, *Phys. Chem. Chem. Phys.*, 2013, **15**, 18627–18634.

17 S. L. Ma, S. H. Zhan, Y. N. Jia and Q. X. Zhou, Superior antibacterial activity of Fe_3O_4-TiO_2 nanosheets under solar light, *ACS Appl. Mater. Interfaces*, 2015, **7**, 21875–21883.

18 Y. J. Yao, F. Lu, Y. P. Zhu, F. Y. Wei, X. T. Liu, C. Lian and S. B. Wang, Magnetic core-shell $CuFe_2O_4$@C_3N_4 hybrids for visible light photocatalysis of Orange II, *J. Hazard. Mater.*, 2015, **297**, 224–233.

19 N. A. Zubir, C. Yacou, J. Motuzas, X. Zhang and X. S. Zhao, The sacrificial role of graphene oxide in stabilising a Fenton-like catalyst GO-Fe_3O_4, *Chem. Commun.*, 2015, **51**, 9291–9293.